ELSEVIER

Contents lists available at ScienceDirect

Energy Storage Materials

journal homepage: www.elsevier.com/locate/ensm





Carbon-binder-domain porosity extraction through lithium-ion battery electrode impedance data

Sergio Pinilla ^{a,1}, Franco M. Zanotto ^{b,c,1}, Diana Zapata Dominguez ^{b,c}, Tomás García ^a, Alejandro A. Franco ^{b,c,d,e,*}

- a Electrochemical Processes Unit, IMDEA Energy, Avda. Ramón de la Sagra 3, Móstoles, Madrid 28935, Spain
- b Laboratoire de Réactivite et Chimie des Solides (LRCS), UMR CNRS 7314, Université de Picardie Jules Verne, Hub de l'Energie, 15, rue Baudelocque, Amiens Cedex 80039. France
- c Réseau sur le Stockage Electrochimique de l'Energie (RS2E), FR CNRS 3459, Hub de L'Energie, 15, rue Baudelocque, Amiens Cedex 80039, France
- d ALISTORE-European Research Institute, FR CNRS 3104, Hub de l'Energie, 15, rue Baudelocque, Amiens Cedex 80039, France
- e Institut Universitaire de France, 103 Boulevard Saint Michel, Paris 75005, France

ARTICLE INFO

Keywords: Li-ion batteries Electrochemical impedance spectroscopy Tortuosity factor Carbon binder domain

ABSTRACT

In the field of 3-D resolved computational modeling of Lithium-ion battery electrodes, the arrangement and properties of the Carbon-Binder-Domain (CBD) play a critical role in the ion and electron transport through their impact on the electrode tortuosity factor. However, until now, the CBD porosity value -its main descriptor affecting its transport properties and occupied volume- has been determined through educated guesses due to the lack of an experimental approach. Here, a novel methodology is reported for the determination of the CBD internal porosity through the combination of computational modeling and experimental electrochemical impedance spectroscopy (EIS). The methodology is based on the creation of a calibration curve that relates tortuosity factor with CBD porosity through digital stochastic generation of electrode microstructures and diffusivity calculations. The curve is then compared to the EIS experimental results and analyzed through a transmission line model, yielding a good estimation of the parameters. In this work, the usefulness and the identified limitation of this approach are demonstrated using three different formulations of LiNi_{0.3}Mn_{0.3}Co_{0.3}O₂ (NMC 111) cathodes. To the best of the authors' knowledge, this is the first reported method for estimating CBD porosity.

1. Introduction

The use of computational modeling has been gaining relevance as a way to reduce cost, time and resources in the innovation process of the battery industry [1]. One of the most impactful ways in which computational modeling has been employed has been in the optimization of the electrode manufacturing process. Electrode manufacturing has a critical role in the performance of the end-devices and even in their aging [2,3]. Electrode thickness, active material size, microstructure and material disposition are just a few of the parameters that have to be considered during the manufacturing process and small changes in composition, deposition and even drying processes can have dire effects on them [4].

For manufacturing related optimizations, 3-D modeling has shown a remarkable flexibility and usefulness. This approach can be used to simulate and optimize the whole pipeline of manufacturing processes including slurry formulation, coating, drying, and calendering [5,6]. It has been even used for the simulation of non-standard manufacturing methods such as solvent-free extrusion [7] or cold pressing [8].

The digital reconstruction in 3-D of an electrode can be done by four differentiated approaches. The first one goes through the simulation of the entire manufacturing process including the formulation, drying, calendering, electrolyte infiltration and electrochemical response, a concept introduced by the ARTISTIC project initiative [9]. This approach is appropriate for understanding the relationship between microstructure parameters and manufacturing process, and solves the relative high computational cost of physics-based models, by combining them with Machine Learning, although this combination implies deriving Machine Learning-surrogate models trained on the

^{*} Corresponding author at: Laboratoire de Réactivite et Chimie des Solides (LRCS), UMR CNRS 7314, Université de Picardie Jules Verne, Hub de l'Energie, 15, rue Baudelocque, Amiens Cedex 80039, France.

E-mail address: alejandro.franco@u-picardie.fr (A.A. Franco).

¹ These authors contributed equally to this work.

physics-based simulation and/or experimental results [10–12]. Another option is the digitalization of experimental electrode microstructures through computer tomography. In this case the fidelity to the experiments is high, but it is resource intensive and, although the active material can generally be properly accounted for, the binder and carbon black (CB) are rarely well captured by this this approach [13]. Third, Neural Network-based generative methods exist that allow the generation of 3D microstructures from single images, [14] but they require significant amount of training data, and they lack a description of the physical processes occurring during the electrode fabrication. The last option is the stochastic generation of electrode microstructures, which will be the use in this work. This method is based on the generation of a backbone of the active material (AM) particles, which is then completed with a phase known as carbon binder domain (CBD) consisting of a combination of the CB and binder. The advantage of this method is its speed and parameter flexibility, which allows exploring a wide range of microstructural parameters. However, it is not able to correlate the electrode microstructure output with a particular set of manufacturing parameters, such as drying rate and calendering pressure.

In all these cases, there is a common challenge, the proper description of the CBD phase. Due to the filament-like structure of the binder and the small size of the CB particles, they tend to combine forming a non-homogeneous hybrid that is challenging for explicit treatment in simulations, thus it becomes necessary to make certain assumptions. These assumptions can have a notable impact on the electrode properties, for instance, Mistry et al. [15] showed computationally that just by changing from a film-like CBD to a finger-like CBD with certain porosity, the kinetic resistance was reduced by 20 % and energy was increased by 2 %. Chouchane et al. [16,17] later explored computationally how different CBD arrangements influenced the performance at different electrode porosities, demonstrating a non-negligible influence in the ionic and electronic response. Moreover, Kroll et al [18] experimentally demonstrated that the CBD phase tends to form aggregates that have a major role in the porous network arrangement and highlighted the importance that the CBD internal structure may have in the ion transport along the electrode.

This CBD internal structure affects both how much space the CBD occupies, and thus how much of the void space it takes from the electrode, and how permeable it is to ion diffusion [19]. Though the importance of the inner structure of the CBD network (specifically the CBD porosity) has been acknowledged, in all works the CBD porosity is still assigned an arbitrary value that is usually between 10 % [7] and 50 % [20], based more on educated guesses rather than experimental determinations. This hinders the fidelity of the electrochemistry simulations, as the CBD porosity can have a substantial impact on the electrode tortuosity factor, which in turn is very decisive on the mass transport processes in the porous network [21]. Throughout this paper, the tortuosity factor, herein denoted τ , will be used as the link between CBD porosity and experimental observables. It should be noted that there is no clear standard in the literature regarding its notation, with some authors using τ for the geometric tortuosity and others using τ for the tortuosity factor. Note that the tortuosity factor is the square of the geometric tortuosity.

There is a wide variety of models that rely on an accurate value of the permeability and volume of the CBD. These can be grouped into manufacturing models [22,23] and performance models [2,24]. For the former, the CBD porosity has an impact on its specific volume and interaction forces between particles. For the latter, it has an impact on its specific volume, ion transport, and electron transport properties. While some of our previously reported manufacturing models are able to account for changes in size of CBD porosity due to the external compression upon electrode calendering, there is no information in experimental literature about the magnitude of this effect. For this reason, the method developed herein considers it independent of calendering parameters.

It is therefore fundamental to develop a reliable way to obtain the CBD porosity value, ϵ . This is exactly the goal of the presented work: we

propose a strategy for determining the CBD porosity combining simulation and experimental efforts. We also consider different electrode formulations and compression degrees to explore the effects of the CBD porosity on the $\tau-\varepsilon$ relationship and use it to compare it with the experimental counterparts. It is important to notice that the CBD structure might depend on the manufacturing method and components. Therefore, the reported values along the paper must be carefully used only in comparable systems and it is encouraged the use of the proposed methodology when attempting to apply it to other electrode chemistries or manufacturing conditions.

2. Methodology

2.1. Experimental

2.1.1. Slurry preparation

NMC based slurries were prepared from raw LiNi $_{0.3}$ Co $_{0.3}$ Mn $_{0.3}$ O $_{2}$ (Ni: Co:Mn=1:1:1) powder (NMC) purchased from MTI corporation. The conductive additive was super C45 carbon black (CB) and the binder was Polyvinylidene Difluoride (PVDF), both also provided by MTI Corporation. The PVDF was pre-mixed with the N-Methyl-2-pyrrolidone (NMP) and homogenized overnight. Subsequently the NMC and CB were added to the mixture in the weight ratios mentioned along the manuscript (90:5:5, 92:4:4 and 95:3:2, NMC:CB:PVDF). After all materials were mixed, NMP was added to the mixture to adjust the solid content to 60 % in weight. The mixing was performed in a vacuum mixer MSK-SFM-7 (MTI corp.) at a fixed mixing speed of 320 rpm. The homogenization of the mixture took place for 5 h in a controlled environment at 20 °C in short steps of 30 min followed by 10 min of rest to avoid the heating up of the sample.

2.1.2. Electrodes preparation

The slurries were coated over a 16 μ m Al foil using a film coater (MSK-AFA-II-VC) with a fixed blade gap of 150 μ m and a coating speed of 0.2 m/min. Previous to the deposition, the rheological properties of the slurry were analyzed with a rheometer (Anton Paar MCR 92). The viscosity vs. shear rate curves are shown in **Fig. S1** where the viscosity for the used coating speed is displayed as well as the calculations to obtain them, **Table S1**. The as-deposited films were immediately dried in a vacuum oven at 60 °C for 4 h. To obtain a precise control of the porosity over the selected range (28 %, 38 % and 48 %) the 12 mm round shaped electrodes were punched before calendering and then individually pressed using a prototype-grade lab press calender (BPN250, People & Technology, Korea). The calendering was performed at constant line speed (0.54 m/min) and 60 °C. The porosity calculations were based on the apparent porosity further described elsewhere [25]

2.1.3. Symmetric cells assembly

The electrodes for the study of the tortuosity factor were assembled in symmetric cell configuration using 2032-coin cells assembled in a dry room with a $\rm H_2O$ content lower than 15 ppm. For the assembly of the cells, a Celgard 2500 separator was used and a 10 mM Tetrabuty-lammonium perchlorate (TBAClO₄) solution prepared in a 1:1 wt% mixture of ethylene carbonate and dimethyl carbonate (EC: DMC) was used as electrolyte, injecting 150 μL per coin cell. The electrolyte conductivity was experimentally determined from the EIS study of symmetric cells consisting of blocking stainless steel electrodes and a range of Celgard 2500 separator stacks (from 1 to 3) with known parameters as described by Landesfeind et al. [26]. The experimental electrolyte conductivity was between 2.4 \times 10 $^{-4}$ S/cm and 3.12 \times 10 $^{-4}$ S/cm at 25 $^{\circ}$ C, matching previous reports [27].

2.1.4. Electrochemical testing

The potentiostatic electrochemical impedance spectroscopy (PEIS) tests were performed with an MTZ-35 impedance analyzer (BioLogic, Seyssinet-Pariset, France) in 0.1 Hz–10 MHz frequency range and a

potential perturbation of 5 mV. All PEIS measurements were performed at 25 $\,^{\circ}\text{C}$ after a week of conditioning of the cells at the testing temperature.

2.1.5. Impedance analysis

The impedance analysis was done with a custom-made Python script which, through a minimization routine, adjusted the experimental impedance data to the equivalent circuit known as transmission line model (TLM), further described in Refs. [13,26,28]. The methodology for the analysis and the tortuosity factor extraction is based on the works of Landesfeind et al. [26] and Pouraghajan et al. [28]. Due to the contact impedance shown by the high porosity electrodes, the use of the TLM-Q model proposed by Landesfeind et al. does not fit well the data. We have therefore used the assumptions described by Pouraghajan et al., considering a transmission line in which there are no effective faradaic reactions due to the blocking-electrolyte, no double-layer effect between current collector and electrolyte, but there is an impedance associated with the contact between the electrode material and current collector ($Z_{\rm CC}$). This leads to the following expression of the electrode impedance ($Z_{\rm E}$):

$$Z_E = R_{ion} \left(Z_{CC} + rac{1}{\sqrt{rac{R_{ion}}{Z_S}} anh \sqrt{rac{R_{ion}}{Z_S}}}
ight)$$
 (1)

where Z_{CC} has been considered a RC circuit, thus being:

$$Z_{CC} = \frac{R_{cc}}{(1 + R_{cc}Q_{cc}(i\omega)^{\gamma})}$$
 (2)

Since we are considering a blocking electrolyte, there is no redox reaction taking place in the active material and therefore there is no charge transfer process associated to it, leading to an expression of Z_S that is purely capacitive:

$$Z_S = \frac{1}{Q_S(i\omega)^{\gamma}} \tag{3}$$

Taking into consideration the cell configuration, the total impedance is:

$$Z = 2Z_E + R_{series} \tag{4}$$

where in R_{series} we are considering the resistance associated with the separator and other possible resistances associated with the cell connection to the potentiostat.

Finally, the tortuosity factor can be estimated through the MacMullin number using the following relationship: [26]

$$\tau = \frac{R_{ion}A\kappa\varepsilon}{d} \tag{5}$$

where κ is the electrolyte conductivity, A is the geometrical area of the electrodes, d is the thickness of the electrodes and ϵ is the porosity.

In order to have sufficient accuracy on the tortuosity factor estimation, six symmetric cells were analyzed per porosity and AM formulation. The electrodes conforming the symmetric cells were paired using their individual thicknesses and porosities, only assembling together those that showed differences lower than 2 μm in thickness and 2 % in porosity. Differences larger than those were leading to significant higher standard deviations in the tortuosity factor values.

2.1.6. Material characterization

The field emission scanning electron microscopy (FE-SEM) images were performed with a JEOL JSM-7900F (JEOL Ltd.). The active material particle size distribution used for the simulations was obtained by adjusting the perimeters of the grains to circumferences through the analysis of SEM images with the ImageJ software. The histograms and

lognormal probability density function of the distribution are displayed in the supporting information section, **Fig. S2**. The cross-sections displayed in **Fig. 2** and used for the size distributions were obtained through the cryofracturing of the electrodes immersed in liquid nitrogen.

2.2. Simulations

2.2.1. Stochastic generation of microstructures

The stochastic generation of microstructures and their characterization were performed with the goal of comparing with experiments. The generated microstructures are composed of three domains, resolved at the micrometer scale: pores, NMC, and CBD. It should be noted that in this model, the pores domain does not account for 100 % of the porosity, since part of it is included in the CBD, but not explicitly described due to its nanometric scale. Periodic boundary conditions were applied along the x and y dimensions, for both generation and characterization. All simulations were carried out by using the GrainGeo and DiffuDict modules of GeoDict 2023 (Math2Market) [29].

Input parameters were taken from experiments whenever possible. Experimental weight percentages were converted to volume percentages by using the values of density from bibliography: 4.78 g cm⁻³ for NMC [30] and 1.8 g cm⁻³ for CBD, [5] before considering its internal porosity. The internal porosity of CBD was left as a parameter for fitting, between the values of 0 % and 60 %. Values much larger than this reach the upper limit for which the whole available volume left by the AM backbone is occupied by CBD. The total porosity values were taken from those determined from the electrodes from their volume and the density of their components. For each of these selected electrodes, the corresponding thickness as measured with calipers was set as the z dimension of the simulation box, resulting in the same mass loading as in experiments. Convergence tests were performed by repeating the whole workflow with increasing system size in the x and y dimensions, repeating each condition three times for different random seeds. It was determined that the deviation in final Deff value was consistently below 1 % for systems larger than 150 μm x 150 μm. While this is acceptable, the final system size was set as 200 µm x 200 µm as a safety margin. The selected voxel size was 0.25 µm, which yielded reliable D_{eff} values. No significant difference was observed for lower values.

To generate the electrodes, spherical NMC particles were randomly placed in the simulation box, following the particle size distribution obtained from the experiment: a LogNormal distribution with a mean diameter of 3.55 μm and a standard deviation of 1.09 μm , with a minimum size of 1 μm and a maximum size of 7 μm (Fig. S2). The volume of NMC was chosen to match the experimental mass loading. Overlap between different particles due to their stochastic placement in the box was removed in a second step, with a tolerance of 0.01 % of the total NMC volume.

In a second step, the CBD was added through the AddBinder function of GrainGeo [31]. This function detects NMC particles that are close to each other and joins them by adding a new phase between them in the shape of a concave meniscus. The shape of the resulting phase depends on the chosen contact angle. Tests with different contact angles revealed no significant difference in the results, therefore the default value of 0° was used. Additionally, the distribution of CBD was assumed to be isotropic, due to the low thickness considered and mild experimental drying rates [32,33]. The volume of CBD added was selected to match the weight percentage of the components, while accounting for the material density and the different selected values of internal CBD porosity; e.g. when internal CBD porosity is set as 50 %, a real density of 1.8 g cm $^{-3}$ is considered as 0.9 g cm $^{-3}$ for the purposes of microstructure generation.

For the purposes of comparing with experiments, between seven and eight NMC microstructures were generated for each electrode composition, totaling 23. For each of them, four different electrodes were generated, with internal CBD porosity varying from 30 % to 60 %.

2.2.2. Characterization of τ of the generated electrodes

In our computational approach, the determination of the tortuosity factor of the electrode by geometrical considerations would be an overestimation, since it does not explicitly account for the internal porous paths within the CBD. For this reason, diffusion simulations were performed to calculate the effective diffusion coefficient of a probe species across the electrode, D_{eff} . From this value, the tortuosity factor τ can be estimated according to Eq. (6):

$$\tau = \frac{D^*}{D_{eff}} \varepsilon \tag{6}$$

where D^* is the diffusion coefficient of the probe species in the open pore phase. This relies on the assumptions that the cross-section area for diffusion through the medium is proportional to porosity, and that the Einstein-Smoluchowski equation holds [34]. These are the same assumptions in which the experimental determination is based on, making comparison appropriate.

An important assumption of this approach concerns the internal structure of the CBD phase. Information on the arrangement of polymer binder and carbon additives is challenging to obtain experimentally [18]. Different models have been proposed to estimate the effective diffusion coefficient of a porous medium from its τ value [35]. In this work, we consider a straightforward model assuming that τ is solely dependent on porosity. Several ways of correlating these two magnitudes have been proposed [36], but among the simplest is the Bruggeman's equation [37,38]

$$\tau = \varepsilon^{1 - \frac{1 + n}{n}} = \varepsilon^{1 - \alpha} \tag{7}$$

where n=2 ($\alpha=1.5$) when the obstacles for diffusion are spheres. This equation, in combination with equation (6), which can be used for the CBD phase, yields

$$D_{eff} = \varepsilon^{1.5} D^* \tag{8}$$

which we use throughout this work. It should be noted that other models for obtaining D_{eff} within the CBD phase could be applied, such as the Maxwell correlation

$$\tau = \frac{3 - \varepsilon}{2} \tag{9}$$

or the generalization of Eq. (7) [39]

$$\tau = \gamma \varepsilon^{1-\alpha} \tag{10}$$

for which empirically determined values of α and γ can be found in literature for different systems [35].

The determination of τ from the synthetic electrodes relies on diffusion equations. Here, Fick's laws of diffusion are considered valid throughout the open pores and the CBD. A steady-state diffusion simulation is carried out in the electrode domain, fixing concentrations of 0 mM and 1 mM of a diffusing probe species at the base and top of the electrode. Periodic boundary conditions are considered in the remaining perpendicular planes. After the steady state concentration and diffusive flux are determined in the simulation domain, the total flux across the electrode, J, can be calculated, and the effective diffusion coefficient calculated as $D_{eff} = |J| \times thickness/1 mM$, where thickness stands for the length of the z dimension of the simulation domain.

3. Results and discussion

As stated in the introduction, the aim of this paper is to develop a method for obtaining the value of the CBD internal porosity. This results section elaborates about the workflow required to carry out this method. In order to serve as a guide for the reader, panel A in Fig. 1 shows a diagram of the steps involved. The workflow consists of two branches

occurring in parallel. The upper row shows the experimental branch, while the lower row presents the branch involving stochastic generation of microstructures and characterization through simulations. Briefly, the method involves determining the tortuosity factor of a set of electrodes manufactured under similar conditions for different calendering situations. This is done through EIS experiments analyzed by means of a TLM. In parallel, electrode microstructures are stochastically generated considering the same compositions and varying CBD porosity values (panel B in Fig. 1). Both results are then fitted to a function of electrode tortuosity factor as a function of electrode porosity, and from the comparison, a value of CBD porosity can be inferred.

First, the simulated microstructures were generated using the size distributions from the experimental electrodes as described in the methods section (Fig. S2). Fig. 2 shows a side-by-side comparison of the SEM images and a slice of the stochastically generated microstructure. It should be noted that the particles in the digital microstructure appear smaller than they are because the slices do not match with the central plane of most particles. The SEM image shows an intermediate grey value as well corresponding to the CBD, concentrated between particles. Panel B shows this domain well represented by the chosen method for the inclusion of CBD in the stochastic microstructure.

An initial analysis of the effect of the internal CBD porosity on the tortuosity factor of the whole electrode is a necessary and insightful first step for the development of the general strategy this work is based on. In this sense, two representative electrodes, with their corresponding porosity and thickness, were chosen and recreated each for different CBD internal porosity values. The high porosity case has a thickness of 38.5 µm and a porosity of 49 %. The low porosity case has a thickness of 54.0 µm and a porosity of 35 %. In each case, the AM particle locations and sizes remain the same, with the volume of CBD varying according to its density. The internal porosity of the CBD ranges from 0 % to 65 %. The results from the determination of tortuosity factors are presented in Fig. 3. The main conclusion arising from this comparison is that as the CBD becomes more porous, less dense, and takes a larger fraction of the available space, the electrode tortuosity factor decreases. In other words, a very extended but very permeable CBD is more favorable for the diffusion of species than an impermeable but very localized CBD. Another conclusion is that this effect is much more impactful in electrodes with lower porosity, for which τ is higher in every case, but varies to a larger degree, from 5.5 to 2.0. This effect anticipates that the determination of CBD internal porosity will be more precise in low porosity electrodes and after calendering. Additionally, these results highlight the importance of an accurate determination of the CBD internal porosity, as its variation has a very significant effect on the tortuosity factor, which in turn is very impactful on transport properties and kinetics [40].

As a next step, following with the lower path of the scheme in Fig. 1, three active material (AM) fractions typically used in lab-scale research and industry for NMC were selected: 90 %, 92 % and 95 %. The experimental preparation of the electrodes is described in the methods section. The resulting final thicknesses after calendering and their corresponding calculated porosities were used to produce their digital counterparts. The results from the characterization of these microstructures are shown on the top row of Fig. 4. The results show the expected trend: for a given value of CBD internal porosity, τ , increases as electrode porosity decreases (corresponding to an increase in compression degree). This agrees with the prediction from Eq. (7) and its generalized form Eq. (10). The irregular intervals between the assessed porosities in these plots are a result of the target values of porosity in the experiments: around 28 %, 38 %, and 48 % and the experimental deviation.

These plots point to a main basis for our proposed method: the trend curve can be approximated as a function of the shape $\tau=\varepsilon^{1-\alpha}$, for a given value of the parameter α that seems to depend on the CBD internal porosity. Note that this equation is in this case used at the electrode level instead of at the internal CBD microstructure level. The continuous line

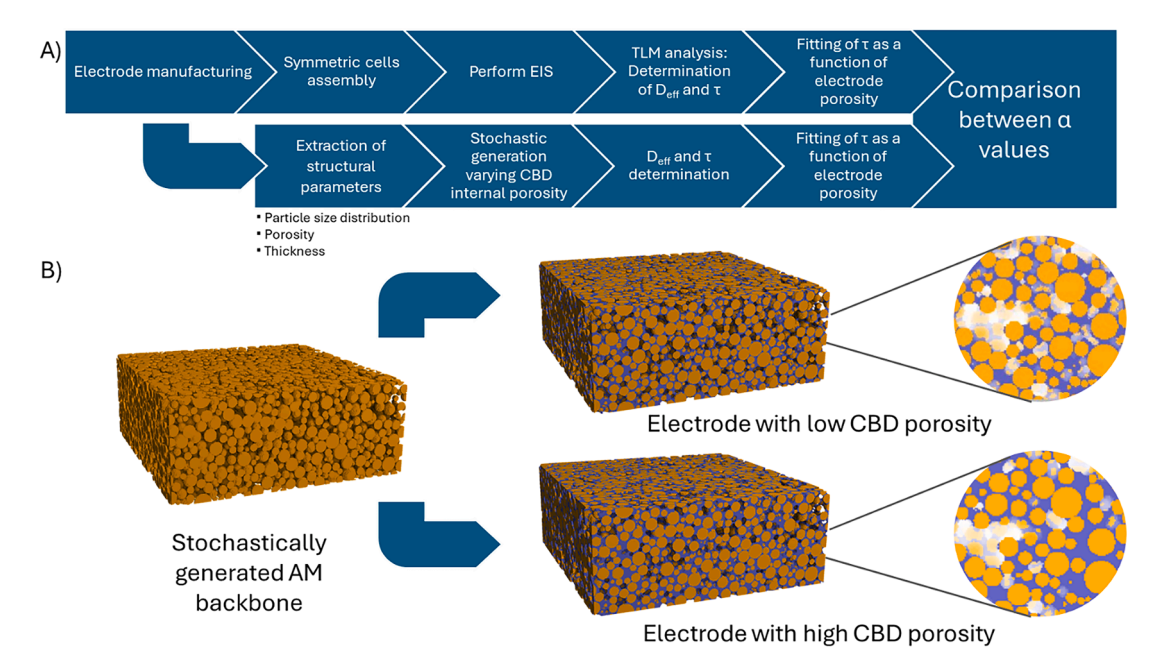


Fig. 1. (A) Schematic representation of the workflow proposed in this paper for the determination of CBD internal porosity. (B) Example of stochastically generated structures, showing that the same backbone of AM particles is used to generate different electrodes according to the user-defined CBD porosity.

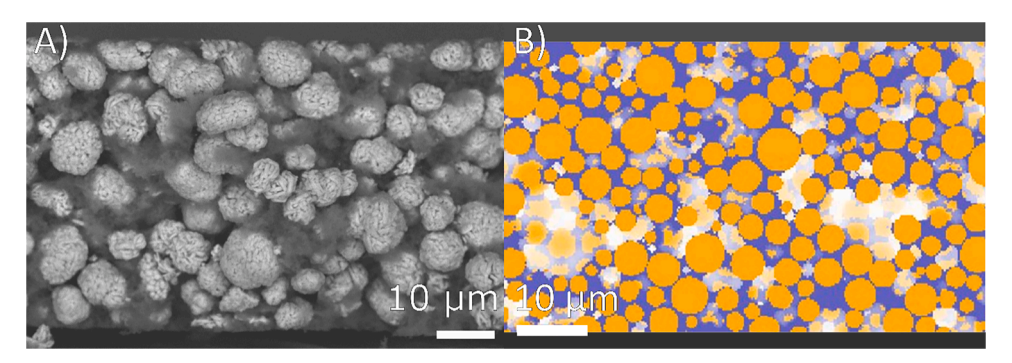


Fig. 2. SEM image of the experimental NMC cathodes with 92 % of active material 4 % of CB and 4 % of PVDF in weight percentages (A) and a sample equivalent microstructure from stochastic generation, with internal CBD porosity of 40 % (B).

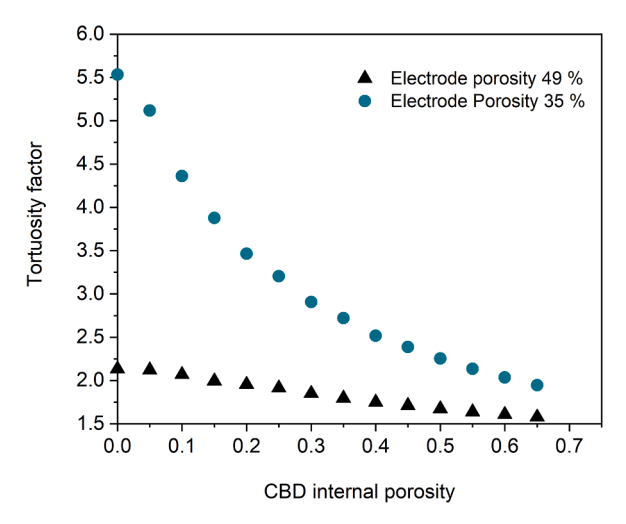


Fig. 3. Dependence of the tortuosity factor with the CBD internal porosity for two fixed electrode porosities according to the simulations performed on stochastically generated microstructures.

shows the best fit for this function, with the values for α presented on the plots in the bottom row. For completeness, the same data is presented in the supporting information section (Fig. S3) but considering the generalized form of this function, Eq. (10). It is noteworthy that all the values of α here determined lie between $\alpha = 1.5$ and $\alpha = 2.0$, which are the expected results for an arrangement of spheres and cylinders, respectively [21]. Furthermore, α closely follows a linear trend, approaching 1.5 for high CBD internal porosity and 2.0 for low CBD internal porosity. This can be interpreted in light of the method used for the addition of the binder material on the microstructure: when the CBD is compact, it is placed joining pairs of AM particles, and acts almost as a wall for diffusion. This results in a network of spheres, joined by low diffusivity cylinders with low aspect ratio. This recalls the model situation resulting in $\alpha = 2.0$. On the other side, when CBD is spread out and very permeable, it occupies a large fraction of the available space, where ion diffusivity follows Eq. (7) with a value of $\alpha = 1.5$.

A relevant point to note is that to fit the data in Fig. 4, Eq. (7) was applied. When considering Eq. (10) instead, *i.e.* λ not necessarily equal to one (Fig. S3), λ values are determined to be between 0.9 and 1.2 (Fig. S4).

To compare the experimental results with the simulations displayed in Fig. 4, the tortuosity of the experimental electrodes was obtained through the impedance analysis described in the methods section and

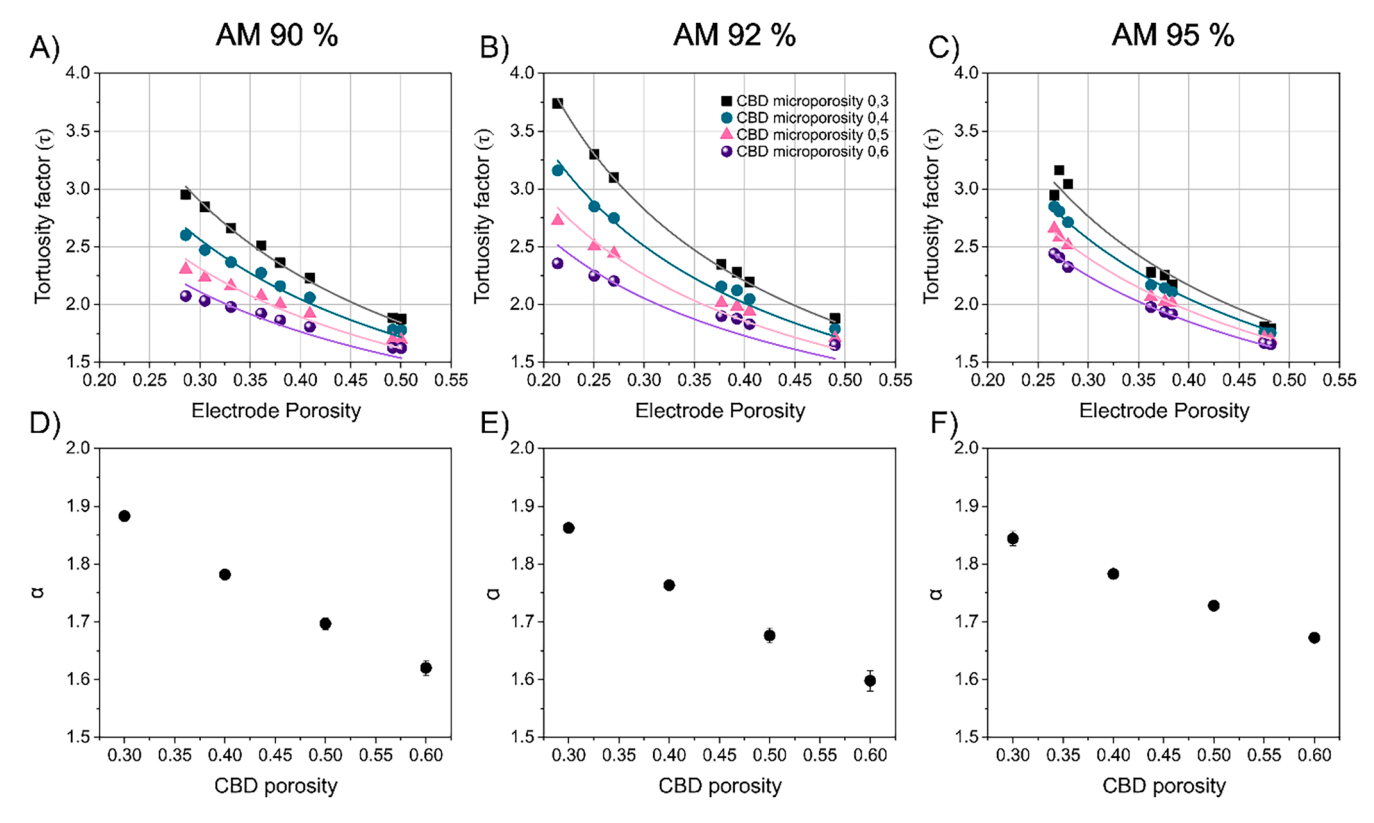


Fig. 4. Simulation of the electrodes tortuosity factors vs. the electrode porosity for a range of CBD porosities ranging from 0.3 to 0.6. The plots on the top row (A to C) include the fitting of the simulation data with the Bruggeman equation (7), for each active material content and CBD porosity. The bottom row (D to F) displays the exponent of the fittings previously described as a function of CBD porosity. All the fitting parameters are detailed in **Table S2**.

schematized in the top row of the scheme in Fig. 1. Three porosity values were selected, 28 %, 38 % and 48 %, for each of the AM percentages and for each porosity, six coin cells in symmetric cell configuration were

produced. All samples for each AM content were cut from the same deposition, and the adjustment of the porosity was done through calendering at different thicknesses. Representative Nyquist plots of the

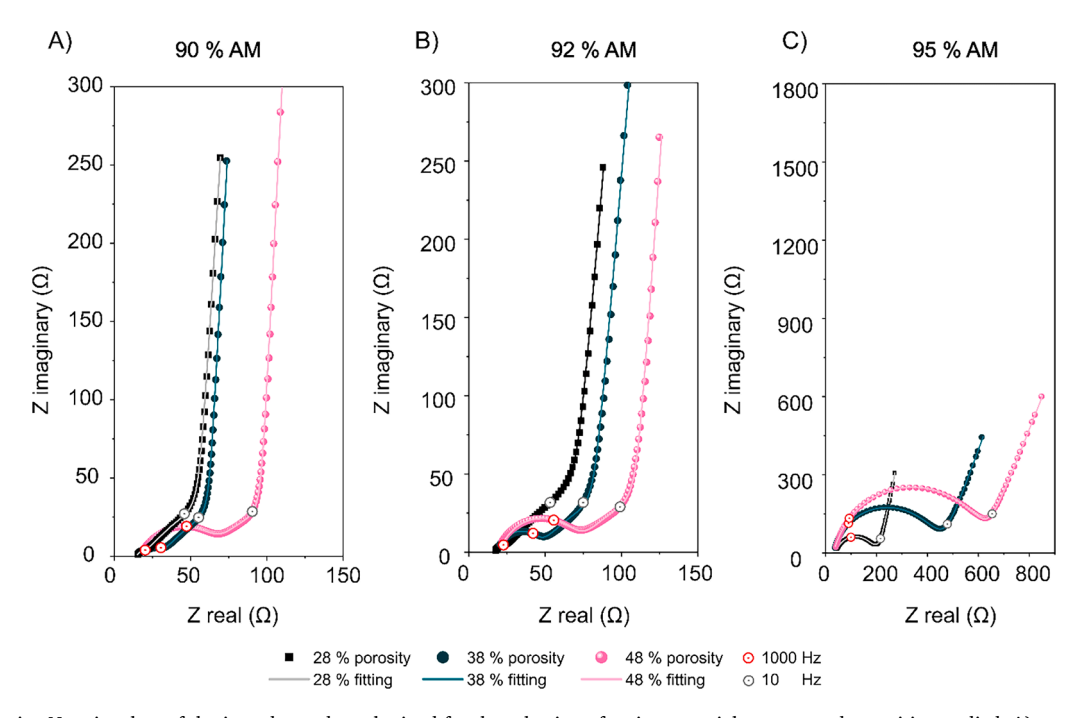


Fig. 5. Representative Nyquist plots of the impedance data obtained for the selection of active material content and porosities studied. A) represents the 90% AM content, B) 92% AM and C) 95% AM. In each of them black dots represent the samples with 28% porosity, black lines the fitting of the data to the TLM and similarly the dark green and pink represents the data for the 38% and 48% porosities respectively. The fitting has been done following the procedure described in the methodology section.

EIS obtained for each porosity and AM content are displayed in Fig. 5.

The behavior of the impedance in the samples with an AM content of 90 % and 92 % is very similar, clearly showing the transmission-line behavior for each porosity range. Interestingly, it can be observed that there is an RC behavior at high frequencies that shows a lower resistance as the porosity is reduced. This RC type shape can be ascribed to the presence of a contact resistance between the porous material and the current collector, as depicted by Pouraghajan et al. [28] and mentioned in the methods section and reflected in Eq. (2). This impedance is not merely in series with the transmission line in the EIS model used but embedded in the transmission line model as portrayed in Eq. (1). The use of this modified transmission line model allows a more accurate determination of the tortuosity factor in electrodes with a significant contact impedance, as it allows to completely disentangle the contributions from the transport along the pores (R_{ton}) and through the current collector – electrode interface (R_{tot}) .

Based on this model, the behavior observed in Fig.5 for the AM 90 % and 92 % can be interpreted as an improvement of the contact between current collector and electrode due to the compression occurred during calendering.

The Nyquist plots of the AM 95 % samples are noticeably different and significantly more difficult to interpret (Fig. 5). For all the porosities, it can be observed that the \mathbf{Z}_{cc} is large enough to completely distort the typical TLM shape. Still, using the modified TLM model previously described, the tortuosity factor of the 28 % porosity samples can be reliably obtained. Although in these samples the \mathbf{Z}_{cc} is dominant in the high frequency range, it still keeps a mostly unaltered TLM shape at low frequencies which allows to obtain \mathbf{R}_{ion} with a low uncertainty.

Oppositely, in the samples with 38 % and 48 % porosities, the large \mathbf{Z}_{cc} shadows and alters the TLM shape as a whole. In these cases, there is not enough information for the model to maintain the same number of parameters and many of them become redundant. This results in unreliable tortuosity factor values lacking physical meaning. These can be observed in Fig. 6, where the tortuosity factor values calculated from the \mathbf{R}_{ion} of the TLM are presented. In the case of the AM 95 % samples, the values corresponding to 28 % porosity are narrowly distributed, while the ones corresponding to 38 % and 48 % present non-coherent values that depend strongly on the initial values.

The contact resistance extracted from the model and represented in **Fig. S5** also show the effect of calendering on the electrode - current collector interface. These values and their trend match quite well with previously reported interface resistance values both from experiments and from simulations [2], and also highlight how the composition of the electrode favors a better contact with the aluminum foil. Additionally, by comparing the reliability of the tortuosity factor extracted with the values of R_{cc} , we see a small gap between the resistances of the 28 % and 38 % porosity for the 95 % AM, corresponding with threshold for the

model reliability. The exact values for the 38 % and 48 % porosities for the 95 % AM must be interpreted with caution because the reliability of the R_{cc} is also affected by the uncertainty of R_{ion} as per Eq. (1). This threshold depends on the manufacturing conditions and experimental setup; therefore, it should be carefully stablished for the system of choice by the means here discussed.

3.1. Derivation of a method for CBD porosity determination

Having analyzed the tortuosity factors of the electrode microstructures generated stochastically and their experimental determination, it is possible now to develop a method for determining CBD internal porosity based on their comparison, as shown in Fig. 1.

A straightforward method that allows a quick estimation is to compare directly the tortuosity factors themselves between the simulations and experiments. It should be noted that there is a set of assumptions in the determination of each of these two values and therefore results will vary accordingly. However, some of the assumptions are the same for both approaches, making comparison appropriate. Fig. 6 shows the experimental results for the electrodes composed of 90 % and 92 % AM according to the treatment presented in the previous subsection along with some of the results from simulations. The results for 95 % AM were not considered due to their high contact resistance and its effect on the tortuosity factor calculation which makes them unreliable. In these plots, the experimental results approximate those of the simulations for 50 % and 60 % internal CBD porosity. Therefore, it can be said that the straightforward comparison method yields a 50-60 % value for the internal porosity of the CBD in the electrodes prepared through the manufacturing method of choice.

Although the data dispersion, especially for the 92 % AM samples, makes this method a rough estimation, we can see that the experimental and simulation data align very well. Experimental tortuosity factor sources always have a wide distribution due to the deviation from the considerations that the methodology requires, such as absolutely equal thicknesses, particle distributions and porosities for both electrodes in the symmetrical cell. In our case, the homogeneity of the 90 % samples were slightly better than those of the 92 %, resulting in a lower dispersion. Still, in all our cases it is well aligned with the tortuosity factor distributions and errors reported in literature for NMC cathodes [13,28].

Additionally, the experimental deviation from the simulation premises, such as the non-perfect sphericity of the real NMC as compared to the simulated, can affect to the estimation of the CBD porosity through simple comparison.

A more quantitative method to estimate the CBD internal porosity from the experimental data is the comparison between the fittings to the Bruggeman equation, Eq. (7), of the stochastic microstructures and the

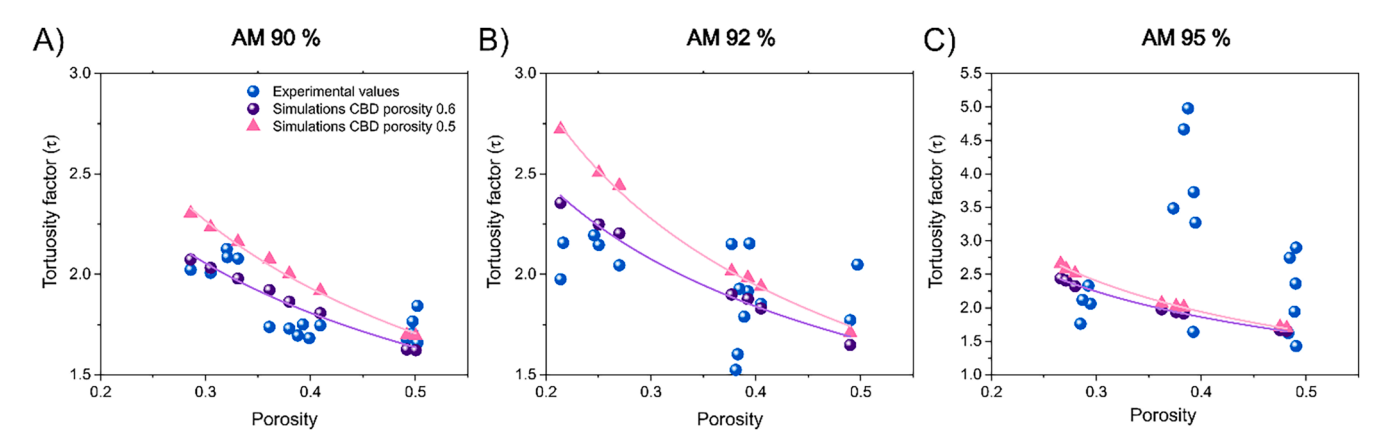


Fig. 6. Experimentally extracted tortuosity values as a function of the electrode porosity for different active material percentages, A to C. The experimental values, in blue, are compared with the closest values from the simulations for different CBD porosities and their fit to equation (7).

experimental ones. As seen in Figs. 4 and 7 the fitting parameters extracted from the simulated microstructures present a linear relationship with the CBD internal porosity within the ranges studied. By fitting the experimental data to the Bruggeman equation as done for the simulations, we can obtain an α value that allows to interpolate from the previous linear relationship to determine the corresponding CBD internal porosity, Fig. 7 C, D. In the particular case of the manufacturing method reported herein, the estimation yields values of $\alpha=1.62\pm0.02$ and $\alpha=1.54\pm0.03$ for 90 % AM and 92 % AM. The interpolation of these results according to the linear fit yield CBD porosity values of 0.59 ± 0.02 and 0.65 ± 0.03 .

These two approaches lead to compatible final results, although the quantitative provides a univocal way to obtain the CBD internal porosity from experimental data. It is important to highlight that the methodology reported and developed in this work is, to the best of our knowledge, the first approach to obtain the equivalent CBD internal porosity from electrochemical experimental determinations. The importance of this value, as shown throughout this paper, can have a very significant influence on the tortuosity factor of the simulated microstructures. It

should be noted that the morphology that the CBD acquires, as well as its internal porosity, are expected to strongly depend on the manufacturing conditions [33,41] as well as on the carbon additive selected [42]. The strategy selected here is presented as an example case for the purposes of a proof of concept. In practice, the user should select the morphology better suited to their experimental conditions. Different tools for the generation of stochastic microstructures that allow different degrees of control of binder morphology are available, such as GeoDict or INNOV [43].

4. Conclusion

We have reported for the first time a methodology to obtain the CBD internal porosity from electrochemical experiments for its use in microstructure-based electrochemical simulations of battery electrodes. Although this work has been done in the framework of positive electrodes for LIB batteries, the methodology here outlined is general to a variety of end-applications where the tortuosity factor of the electrode microstructure plays a major role in the performance, such as other

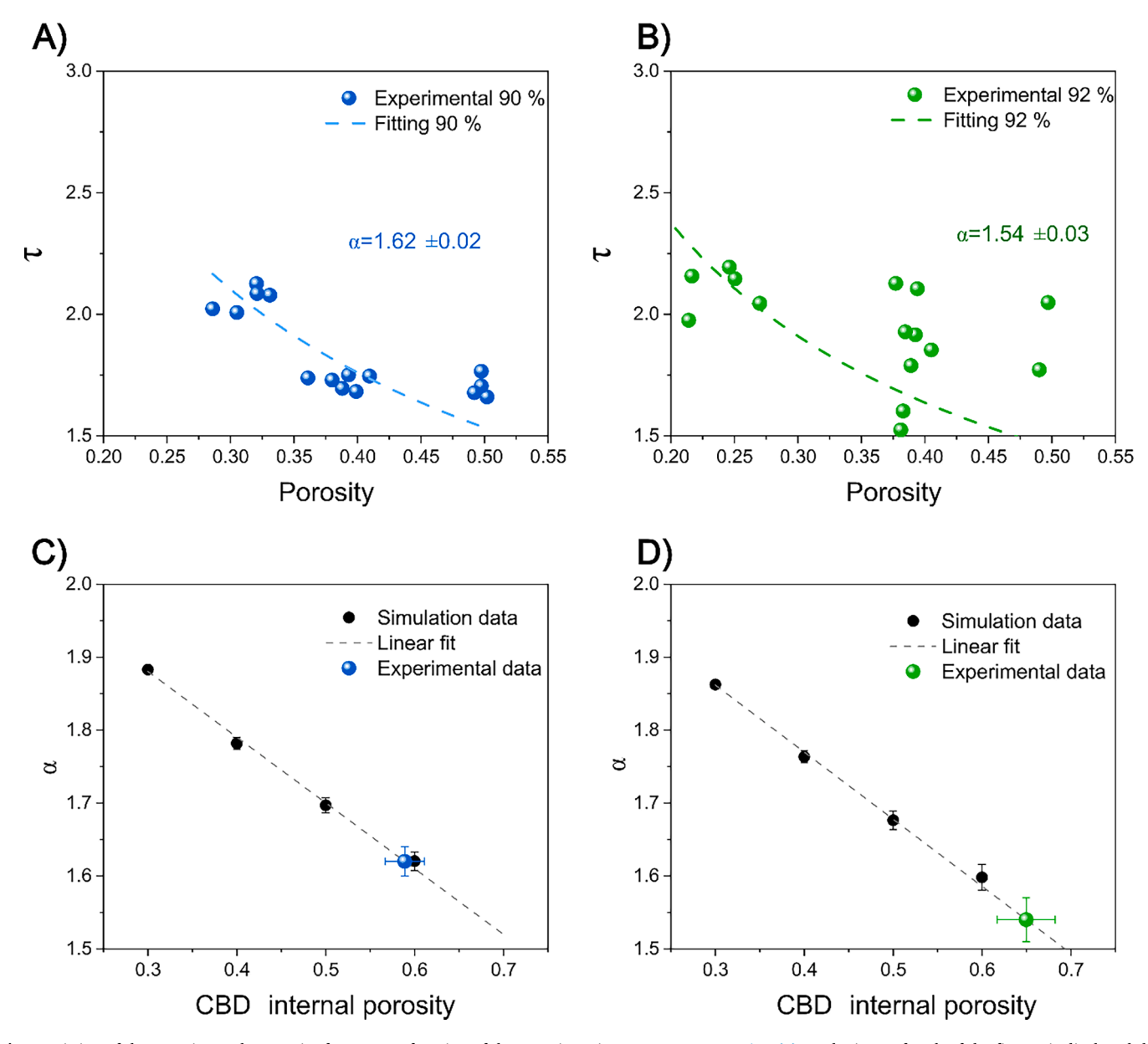


Fig. 7. Fitting of the experimental tortuosity factors as a function of the porosity using Bruggeman equation (7). In the inset of each of the figures is displayed the alpha value extracted from the fittings. Further detail of the fitting parameters can be found in **Table S3**.

battery chemistries and fuel cells [23,44].

As a case study, we have used NMC111 positive electrodes with 90 %, 92 %, and 95 % active material content, aiming for porosities of 28 %, 38 %, and 48 %. We determined that samples with low electrical conductivity, i.e. for high AM content and porosity, are less useful for this approach. This is because high contact resistances prevent reliable tortuosity factor estimations from impedance data, which limit the study of certain electrodes formulations. The determined values for internal CBD porosity were 0.59 ± 0.02 and 0.65 ± 0.03 for electrodes with 90 % and 92 % AM composition. However, these values are expected to depend strongly on manufacturing conditions, particularly during mixing and drying.

The methodology reported is schematized in Fig. 1 and can be summarized as follows. First, experimental electrodes must be produced, and through different calendering thicknesses, a range of porosities values are obtained. The tortuosity factors of electrodes with different porosities are determined by assembling symmetric cells with a blocking electrolyte and analyzing their impedance using a transmission line model suited to the experimental system. At this step it is important that the adherence of the electrode with the current collector is as good as possible, otherwise the range of exploitable electrode porosities will be severely reduced due to an excessive contact resistance at high porosities. Once all the experimental information is obtained, equivalent virtual electrodes are generated using the experimentally determined thickness, particle size distribution, formulation, mass loading and total porosities. A large enough electrode microstructure must be generated per set of parameters to reduce the dependence on the random seed used for stochastic generation. These generations have to be repeated with varying CBD internal porosity values, obtaining for each of them the tortuosity factor as a function of the total electrode porosity. Afterwards, each tortuosity factor vs. electrode porosity dataset should be fitted to either the Bruggeman equation, its generalized form, or another appropriate model. Comparing the fitting parameters of the simulations to those of the experimental set, the CBD internal porosity that best matches the experimental results corresponds to the one of the real electrode. This microstructure can then be used to simulate the endapplication of interest with the certainty that the tortuosity factor will be matching its experimental counterpart.

Data availability statement

The data that support the findings of this study are available from the corresponding author upon reasonable request.

Supporting Information

Supporting Information is available from the Wiley Online Library or from the author.

CRediT authorship contribution statement

Sergio Pinilla: Writing – original draft, Visualization, Validation, Project administration, Methodology, Investigation, Funding acquisition, Formal analysis, Data curation, Conceptualization. Franco M. Zanotto: Writing – original draft, Visualization, Validation, Software, Methodology, Investigation, Formal analysis, Data curation, Conceptualization. Diana Zapata Dominguez: Writing – review & editing, Investigation. Tomás García: Writing – review & editing, Investigation. Alejandro A. Franco: Writing – review & editing, Supervision, Project administration, Methodology, Funding acquisition, Conceptualization.

Declaration of competing interest

The authors declare that they have no known competing financial interests or personal relationships that could have appeared to influence the work reported in this paper.

Acknowledgments

S.P. and T.G. gratefully acknowledge financial support from "Comunidad de Madrid" to the project ADEMOSSBat (2022-T1/IND-23776). A.A.F. and F.M.Z. acknowledge the European Union's Horizon Europe research and innovation programme under grant agreement No. 101069686 (PULSELION). A.A.F. and D.Z.D. acknowledge the European Union's Horizon 2020 research and innovation program for the funding support through the European Research Council (grant agreement 772873, "ARTISTIC" project). A.A.F. acknowledges the European Research Council for the funding support through the ERC Proof-of-Concept grant No. 101069244 (SMARTISTIC project). A.A.F. acknowledges Institut Universitaire de France for the support.

Supplementary materials

Supplementary material associated with this article can be found, in the online version, at doi:10.1016/j.ensm.2024.103818.

References

- A.A. Franco, A. Rucci, D. Brandell, C. Frayret, M. Gaberscek, P. Jankowski, P. Johansson, Boosting rechargeable batteries R&D by multiscale modeling: myth or reality? Chem. Rev. 119 (2019) 4569–4627, https://doi.org/10.1021/acs. chemrev.8b00239.
- [2] C. Liu, T. Lombardo, J. Xu, A.C. Ngandjong, A.A. Franco, An experimentally-validated 3D electrochemical model revealing electrode manufacturing parameters' effects on battery performance, Energy Storage Mater. 54 (2023) 156–163, https://doi.org/10.1016/j.ensm.2022.10.035.
- [3] M.M. Titirici, P. Johansson, M. Crespo Ribadeneyra, H. Au, A. Innocenti, S. Passerini, E. Petavratzi, P. Lusty, A.A. Tidblad, A.J. Naylor, R. Younesi, Y. A. Chart, J. Aspinall, M. Pasta, J. Orive, L.M. Babual, M. Reynaud, K.G. Latham, T. Hosaka, S. Komaba, J. Bitenc, A. Ponrouch, H. Zhang, M. Armand, R. Kerr, P. C. Howlett, M. Forsyth, J. Brown, A. Grimaud, M. Vilkman, K.B. Dermenci, S. Mousavihashemi, M. Berecibar, J.E. Marshall, C.R. McElroy, E. Kendrick, T. Safdar, C. Huang, F.M. Zanotto, J.F. Troncoso, D.Z. Dominguez, M. Alabdali, U. Vijay, A.A. Franco, S. Pazhaniswamy, P.S. Grant, S. Lopez Guzman, M. Fehse, M. Galceran Mestres, N. Antuñano, 2024 roadmap for sustainable batteries, J. Phys. Energy (2024), https://doi.org/10.1088/2515-7655/ad6bc0.
- [4] P.S. Grant, D. Greenwood, K. Pardikar, R. Smith, T. Entwistle, L.A. Middlemiss, G. Murray, S.A. Cussen, M.J. Lain, M.J. Capener, M. Copley, C.D. Reynolds, S. D. Hare, M.J.H. Simmons, E. Kendrick, S.P. Zankowski, S. Wheeler, P. Zhu, P. R. Slater, Y.S. Zhang, A.R.T. Morrison, W. Dawson, J. Li, P.R. Shearing, D.J.L. Brett, G. Matthews, R. Ge, R. Drummond, E.C. Tredenick, C. Cheng, S.R. Duncan, A. M. Boyce, M. Faraji-Niri, J. Marco, L.A. Roman-Ramirez, C. Harper, P. Blackmore, T. Shelley, A. Mohsseni, D.J. Cumming, Roadmap on Li-ion battery manufacturing research, J. Phys. Energy 4 (2022) 042006, https://doi.org/10.1088/2515-7655/ac8e30.
- [5] A.C. Ngandjong, T. Lombardo, E.N. Primo, M. Chouchane, A. Shodiev, O. Arcelus, A.A. Franco, Investigating electrode calendering and its impact on electrochemical performance by means of a new discrete element method model: Towards a digital twin of Li-Ion battery manufacturing, J. Power Sources 485 (2021) 229320, https://doi.org/10.1016/j.jpowsour.2020.229320.
- [6] A.C. Ngandjong, A. Rucci, M. Maiza, G. Shukla, J. Vazquez-Arenas, A.A. Franco, Multiscale simulation platform linking lithium ion battery electrode fabrication process with performance at the cell level, J. Phys. Chem. Lett. 8 (2017) 5966–5972, https://doi.org/10.1021/acs.jpclett.7b02647.
- [7] B. Paredes-Goyes, F.M. Zanotto, V. Boudeville, S. Grugeon, L. Dupont, A.A. Franco, Mesoscopic model of extrusion during solvent-free lithium-ion battery electrode manufacturing**, batter. Supercaps 7 (2024) e202300441. 10.1002/batt. 202300441
- [8] M. Alabdali, F.M. Zanotto, M. Chouchane, A.C. Ngandjong, V. Viallet, V. Seznec, Y. S. Meng, A.A. Franco, Understanding mechanical stresses upon solid-state battery electrode cycling using discrete element method, Energy Storage Mater. 70 (2024) 103527, https://doi.org/10.1016/j.ensm.2024.103527.
- [9] J.F. Troncoso, F.M. Zanotto, D.E. Galvez-Aranda, D.Z. Dominguez, L. Denisart, A. A. Franco, The ARTISTIC battery manufacturing digitalization initiative: from fundamental research to industrialization, Batter, Supercaps (2024) e202400385, https://doi.org/10.1002/batt.202400385.
- [10] D.E. Galvez-Aranda, T.L. Dinh, U. Vijay, F.M. Zanotto, A.A. Franco, Time-dependent deep learning manufacturing process model for battery electrode microstructure prediction, Adv. Energy Mater. 14 (2024) 2400376, https://doi.org/10.1002/aenm.202400376.
- [11] M. Duquesnoy, C. Liu, D.Z. Dominguez, V. Kumar, E. Ayerbe, A.A. Franco, Machine learning-assisted multi-objective optimization of battery manufacturing from synthetic data generated by physics-based simulations, Energy Storage Mater. 56 (2023) 50–61, https://doi.org/10.1016/j.ensm.2022.12.040.
- [12] M. Duquesnoy, C. Liu, V. Kumar, E. Ayerbe, A.A. Franco, Toward high-performance energy and power battery cells with machine learning-based optimization of

- electrode manufacturing, J. Power Sources 590 (2024) 233674, https://doi.org/
- [13] J. Landesfeind, M. Ebner, A. Eldiven, V. Wood, H.A. Gasteiger, Tortuosity of battery electrodes: validation of impedance-derived values and critical comparison with 3D tomography, J. Electrochem. Soc. 165 (2018) A469–A476, https://doi. org/10.1149/2.0231803jes.
- [14] S. Kench, S.J. Cooper, Generating three-dimensional structures from a two-dimensional slice with generative adversarial network-based dimensionality expansion, Nat. Mach. Intell. 3 (2021) 299–305, https://doi.org/10.1038/s42256-021-00322-1.
- [15] A.N. Mistry, K. Smith, P.P. Mukherjee, Secondary-phase stochastics in lithium-ion battery electrodes, ACS Appl. Mater. Interfaces 10 (2018) 6317–6326, https://doi. org/10.1021/acsami.7b17771.
- [16] M. Chouchane, A.A. Franco, Deconvoluting the impacts of the active material skeleton and the inactive phase morphology on the performance of lithium ion battery electrodes, Energy Storage Mater. 47 (2022) 649–655, https://doi.org/ 10.1016/j.enm.2022.02.016
- [17] M. Chouchane, A. Rucci, T. Lombardo, A.C. Ngandjong, A.A. Franco, Lithium ion battery electrodes predicted from manufacturing simulations: Assessing the impact of the carbon-binder spatial location on the electrochemical performance, J. Power Sources 444 (2019) 227285, https://doi.org/10.1016/j.jpowsour.2019.227285.
- [18] M. Kroll, S.L. Karstens, M. Cronau, A. Höltzel, S. Schlabach, N. Nobel, C. Redenbach, B. Roling, U. Tallarek, Three-phase reconstruction reveals how the microscopic structure of the carbon-binder domain affects ion transport in lithiumion batteries, Batter. Supercaps 4 (2021) 1363–1373, https://doi.org/10.1002/ bett 2021.00077
- [19] M. Chouchane, A.A. Franco, About the consideration of the inactive materials and the meshing procedures in computational models of lithium ion battery electrodes, ChemElectroChem. 9 (2022) e202200692, https://doi.org/10.1002/ celc.202200692.
- [20] M. Chouchane, E.N. Primo, A.A. Franco, Mesoscale effects in the extraction of the solid-state lithium diffusion coefficient values of battery active materials: physical insights from 3D modeling, J. Phys. Chem. Lett. 11 (2020) 2775–2780, https://doi. org/10.1021/acs.ipclett.0c00517.
- [21] L. Holzer, P. Marmet, M. Fingerle, A. Wiegmann, M. Neumann, V. Schmidt, Tortuosity and Microstructure Effects in Porous Media: Classical Theories, Empirical Data and Modern Methods, Springer International Publishing, Cham, 2023. https://doi.org/10.1007/978-3-031-30477-4.
- [22] T. Lombardo, F. Caro, A.C. Ngandjong, J. Hoock, M. Duquesnoy, J.C. Delepine, A. Ponchelet, S. Doison, A.A. Franco, The ARTISTIC online calculator: exploring the impact of lithium-ion battery electrode manufacturing parameters interactively through your browser, Batter. Supercaps 5 (2022) e202100324, https://doi.org/ 10.1002/batt.202100324.
- [23] T. Lombardo, F. Lambert, R. Russo, F.M. Zanotto, C. Frayret, G. Toussaint, P. Stevens, M. Becuwe, A.A. Franco, Experimentally validated three-dimensional modeling of organic-based sodium-ion battery electrode manufacturing, Batter. Supercaps 5 (2022) e202200116, https://doi.org/10.1002/batt.202200116.
- [24] A. Shodiev, M. Chouchane, M. Gaberscek, O. Arcelus, J. Xu, H. Oularbi, J. Yu, J. Li, M. Morcrette, A.A. Franco, Deconvoluting the benefits of porosity distribution in layered electrodes on the electrochemical performance of Li-ion batteries, Energy Storage Mater. 47 (2022) 462–471, https://doi.org/10.1016/j.ensm.2022.01.058.
- [25] S. Pinilla, S. Ryan, L. McKeon, M. Lian, S. Vaesen, A. Roy, W. Schmitt, J. N. Coleman, V. Nicolosi, Additive manufacturing of Li-ion batteries: a comparative study between electrode fabrication processes, Adv. Energy Mater. (2023) 2203747. https://doi.org/10.1002/aenm.202203747.
- [26] J. Landesfeind, J. Hattendorff, A. Ehrl, W.A. Wall, H.A. Gasteiger, Tortuosity determination of battery electrodes and separators by impedance spectroscopy, J. Electrochem. Soc. 163 (2016) A1373–A1387, https://doi.org/10.1149/ 2.1141607jes.
- [27] D.Zapata Dominguez, B. Mondal, M. Gaberscek, M. Morcrette, A.A. Franco, Impact of the manufacturing process on graphite blend electrodes with silicon

- nanoparticles for lithium-ion batteries, J. Power Sources 580 (2023) 233367, https://doi.org/10.1016/j.jpowsour.2023.233367.
- [28] F. Pouraghajan, H. Knight, M. Wray, B. Mazzeo, R. Subbaraman, J. Christensen, D. Wheeler, Quantifying tortuosity of porous Li-ion battery electrodes: comparing polarization-interrupt and blocking-electrolyte methods, J. Electrochem. Soc. 165 (2018) A2644–A2653, https://doi.org/10.1149/2.0611811jes.
- [29] Math2Market GmbH J. Becker, F. Biebl, L. Cheng, E. Glatt, A. Grießer, M. Groß, S. Linden, D. Mosbach, C. Wagner, A. Weber, R. Westerteiger, A. Wiegmann, A. Neundorf, GeoDict Releases 2024, Math2Market GmbH, DE, 2024, https://doi. org/10.30423/release.geodict2024 (accessed May 23, 2024).
- [30] Y. Chen, J. Key, K. O'Regan, T. Song, Y. Han, E. Kendrick, Revealing the rate-limiting electrode of lithium batteries at high rates and mass loadings, Chem. Eng. J. 450 (2022) 138275, https://doi.org/10.1016/j.cej.2022.138275.
- [31] J. Hilden, S. Rief, B. Planas, GeoDict 2024 User Guide, Math2Market GmbH, Germany, 2023, https://doi.org/10.30423/userguide.geodict. . GrainGeo handbook(accessed May 24, 2024).
- [32] J. Kumberg, M. Müller, R. Diehm, S. Spiegel, C. Wachsmann, W. Bauer, P. Scharfer, W. Schabel, Drying of lithium-ion battery anodes for use in high-energy cells: influence of electrode thickness on drying time, adhesion, and crack formation, Energy Technol 7 (2019) 1900722, https://doi.org/10.1002/ente.201900722.
- [33] T. Lombardo, A.C. Ngandjong, A. Belhcen, A.A. Franco, Carbon-binder migration: a three-dimensional drying model for lithium-ion battery electrodes, Energy Storage Mater. 43 (2021) 337–347, https://doi.org/10.1016/j.ensm.2021.09.015.
- [34] M. Ebner, V. Wood, Tool for tortuosity estimation in lithium ion battery porous electrodes, J. Electrochem. Soc. 162 (2015) A3064–A3070, https://doi.org/ 10.1149/2.0111502ies.
- [35] B. Tjaden, D.J.L. Brett, P.R. Shearing, Tortuosity in electrochemical devices: a review of calculation approaches, Int. Mater. Rev. 63 (2018) 47–67, https://doi. org/10.1080/09506608.2016.1249995.
- [36] L. Shen, Z. Chen, Critical review of the impact of tortuosity on diffusion, Chem. Eng. Sci. 62 (2007) 3748–3755, https://doi.org/10.1016/j.ces.2007.03.041.
- [37] B. Tjaden, S.J. Cooper, D.J. Brett, D. Kramer, P.R. Shearing, On the origin and application of the Bruggeman correlation for analysing transport phenomena in electrochemical systems, Curr. Opin. Chem. Eng. 12 (2016) 44–51, https://doi. org/10.1016/j.coche.2016.02.006.
- [38] D.A.G. Bruggéman, Berechnung verschiedener physikalischer Konstanten von heterogenen substanzen. I. Dielektrizitätskonstanten und leitfähigkeiten der mischkörper aus isotropen substanzen, Ann. Phys. 416 (1935) 665–679, https:// doi.org/10.1002/andp.19354160802.
- [39] I.V. Thorat, D.E. Stephenson, N.A. Zacharias, K. Zaghib, J.N. Harb, D.R. Wheeler, Quantifying tortuosity in porous Li-ion battery materials, J. Power Sources 188 (2009) 592–600, https://doi.org/10.1016/j.jpowsour.2008.12.032.
- [40] B. Delattre, R. Amin, J. Sander, J. De Coninck, A.P. Tomsia, YM. Chiang, Impact of pore tortuosity on electrode kinetics in lithium battery electrodes: study in directionally freeze-Cast LiNi_{0.8} Co_{0.15} Al_{0.05} O₂ (NCA), J. Electrochem. Soc. 165 (2018) A388–A395. https://doi.org/10.1149/2.1321802ies.
- [41] J. Entwistle, R. Ge, K. Pardikar, R. Smith, D. Cumming, Carbon binder domain networks and electrical conductivity in lithium-ion battery electrodes: A critical review, Renew. Sustain. Energy Rev. 166 (2022) 112624, https://doi.org/ 10.1016/j.rser.2022.112624
- [42] X. Lu, G.J. Lian, J. Parker, R. Ge, M.K. Sadan, R.M. Smith, D. Cumming, Effect of carbon blacks on electrical conduction and conductive binder domain of nextgeneration lithium-ion batteries, J. Power Sources 592 (2024) 233916, https://doi. org/10.1016/j.jpowsour.2023.233916.
- [43] M. Chouchane, A.A. Franco, An invitation to engage with computational modeling: user-friendly tool for in silico battery component generation and meshing, Batter. Supercaps 4 (2021) 1451–1456, https://doi.org/10.1002/batt.202100096.
- [44] M. Alabdali, F.M. Zanotto, M. Duquesnoy, AK. Hatz, D. Ma, J. Auvergniot, V. Viallet, V. Seznec, A.A. Franco, Three-dimensional physical modeling of the wet manufacturing process of solid-state battery electrodes, J. Power Sources 580 (2023) 233427, https://doi.org/10.1016/j.jpowsour.2023.233427.